InP-based polarization rotator-splitter for mid-infrared photonic integration circuits

Cite as: AIP Advances **9**, 015303 (2019); https://doi.org/10.1063/1.5055863
Submitted: 11 September 2018 . Accepted: 26 December 2018 . Published Online: 09 January 2019

Chi-Jui Chung, Jason Midkiff, Kyoung Min Yoo, Ali Rostamian, Joel Guo, Ray T. Chen, and Swapnajit Chakravarty

InP-based polarization rotator-splitter for mid-infrared photonic integration circuits

Cite as: AIP Advances 9, 015303 (2019); doi: 10.1063/1.5055863
Submitted: 11 September 2018 • Accepted: 26 December 2018 •
Published Online: 9 January 2019

Chi-Jui Chung,[1,a)] Jason Midkiff,[2] Kyoung Min Yoo,[1] Ali Rostamian,[1] Joel Guo,[1] Ray T. Chen,[1,2,a)] and Swapnajit Chakravarty[2,a)]

AFFILIATIONS

[1]Microelectronic Research Center, Department of Electronical and Computer Engineering, The University of Texas, Austin, Texas 78758, USA

[2]Omega Optics, Inc., 8500 Shoal Creek Blvd., Austin, Texas 78757, USA

[a)]**Electronic mail:** cjchung@utexas.edu, swapnajit.chakravarty@omegaoptics.com, and chen@ece.utexas.edu.

ABSTRACT

We design and experimentally demonstrate the propagation loss of waveguides and the operation of a single-step etched polarization rotator-splitter (PRS) in low index contrast InGaAs-InP material system at 6.15 μm. Propagation losses 4.19 dB/cm for TM mode and 3.25 dB/cm for TE mode are measured. The designed PRS can achieve near 100% conversion efficiency. This study enables the possibility of monolithic integration of quantum cascade devices with TM-polarized characteristics and TE-guiding two-dimensional slotted photonic crystal waveguide gas sensors for on-chip monolithic absorption spectroscopy.

Mid-infrared (Mid-IR) absorption spectroscopy based on integrated photonic circuits has shown great promise in trace-gas sensing[1] applications in which the mid-IR radiation directly interacts with the targeted analyte. This approach eliminates the needs of bulky gas cells and free-space optical components. Therefore, it has substantial advantages such as being lightweight, alignment-free, and offering high sensitivity sensing over conventional off-chip methods.[2,3] In addition, on-chip slow light enhanced slotted photonic crystal waveguides (PCWs) have been demonstrated to effectively increase light-matter interaction lengths and therefore higher detection sensitivity for the targeted gas analyte can be realized.[4,5] An ideal spectrometer needs to cover the entire molecular fingerprint region from λ= 3-15 μm. Although silicon is the material of choice for most passive photonic applications, it is not suitable for wavelengths λ> 6 μm due to its high intrinsic material loss. Germanium and GaAs are suitable for covering the above wavelength range. However, in the design of integrated photonic spectrometers, we must also take into consideration that the light source in the mid-IR is primarily in the form of quantum cascade lasers (QCLs). The best performing room temperature mid-IR QCLs have been demonstrated till date in the InP material system. Three approaches exist for the integration of light sources and detectors with passive photonics. The first method includes a heterogeneous material integration of individual laser, detector and passive photonic waveguide. The heterogeneous integration procedure requires precise free-space optical alignments and very elaborate packaging process which introduces fragility and additional cost for portable sensing applications in harsh environments. The second method involves bonding between III-V QCL epitaxial layers and silicon layers via an appropriate interface with silicon dioxide or polymer that is typically characterized by high optical losses in almost the entire wavelength range mentioned above. The third method involves monolithic integration where the passive photonics and the active quantum cascade laser/detector are fabricated on a bonding-free single epitaxially grown InP platform. The third method requires an epitaxial process to grow QCL/QCD layers along with the waveguide layers but essentially avoids till date high-cost and low-yield wafer/die bonding processes. At the same time, monolithic integration provides a low loss waveguiding platform with InGaAs core and InP cladding materials with material losses < 2 dB/cm in the λ= 3-15 μm

wavelength range. A photonic integration platform requires various passive photonic components such as waveguides,[6] switches,[7] and modulators,[8] with active components such as lasers,[9] detectors,[10] and electronics,[11] all of which have been experimentally demonstrated in the InP platform in the near-infrared (near-IR) but not necessarily for mid-IR range.

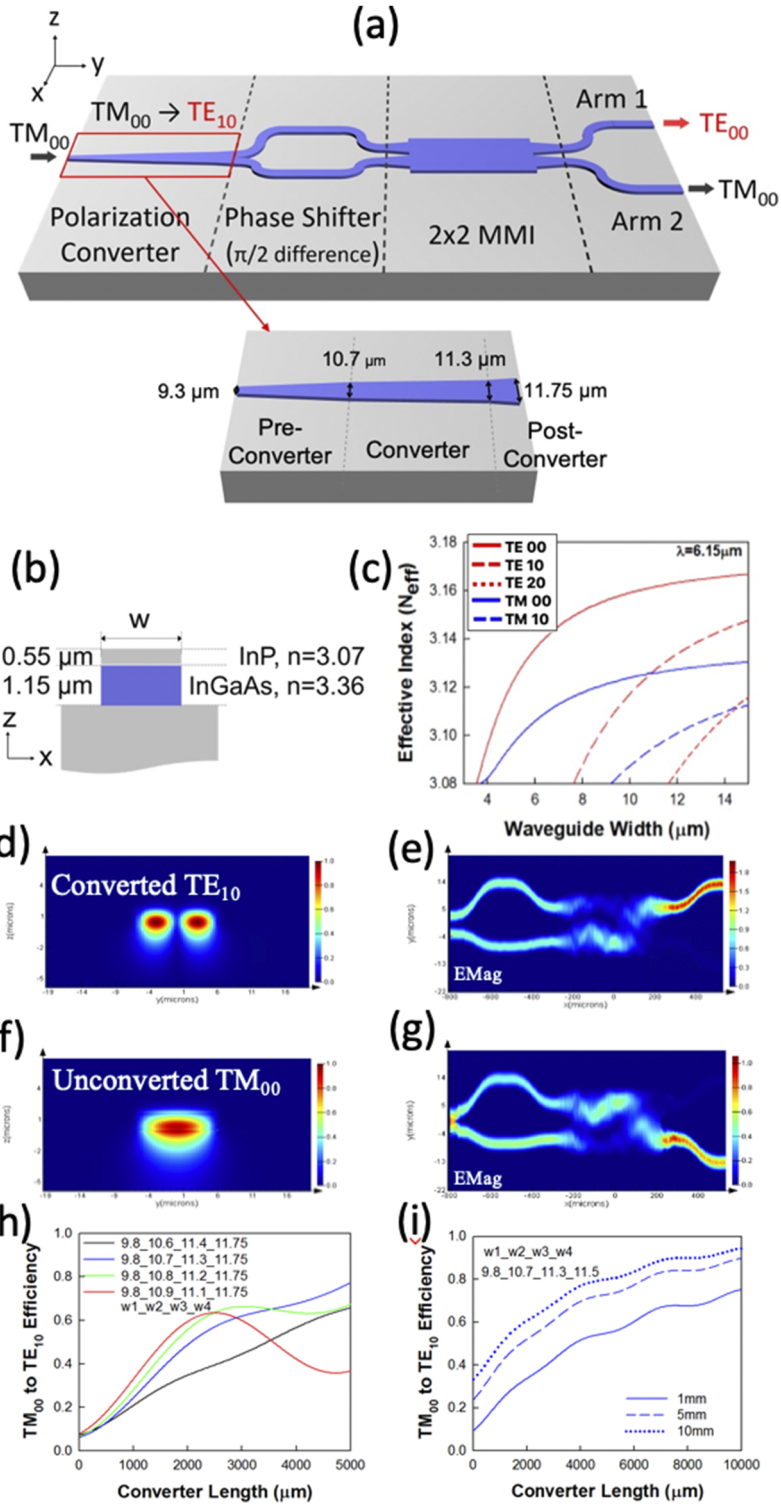

FIG. 1. (a) Schematic diagram of the single-step etched polarization rotator-splitter (PRS) operating at 6.15 μm in InGaAs-InP platform. Inset shows the details of the TM_{00} to TE_{10} conversion section, including pre-converter, converter and post-converter sections. (b) cross-section schematic and the epitaxy layer structures of the PRS, (c) the effective index versus InGaAs-InP waveguide width plot, (d) (e) modal distribution of converted TE_{10}, and (f) (g) modal distribution of unconverted TM_{00}. (h) Simulated conversion efficiency versus length of the converter section with converter width tolerance analysis. w1 to w4 are the widths at beginning of pre-converter, beginning of converter, beginning of post-converter and end of post converter respectively. (i) converter efficiency with different lengths of the pre-converter.

In our final desired application of a monolithic spectrometer, a PRS is needed on the input end to couple the transverse magnetic (TM) polarized emission from a QCL into previous demonstrated high sensitivity two-dimensional slotted PCWs that exhibit slow light effects and enhanced sensitivity for only the transverse electric (TE) polarization. The PRS on the output end converts the polarization back to TM for detection by a monolithically integrated quantum cascade detector. Therefore, the PRS is the essential component which helps integration with PCWs and thus enables high sensitivity trace gas sensing in a monolithic photonic integration architecture. Various designs of near-IR polarization rotators have been reported in the literature.[12] Among those designs, some of them such as the dual-etched polarization rotator designs,[13–16] require an extra masking/alignment step and thus have tight fabrication tolerance. In this paper, we provide a proof-of-concept experimental demonstration of a single-step etched polarization rotator-splitter (PRS) to eliminate the extra step in the InGaAs/InP platform in the mid-IR. We first characterize the losses for both TM and TE polarization in fabricated waveguides and bends in the InGaAs-InP platform. Higher propagation loss data are observed in TM mode propagation due to the smaller refractive contrast in the vertical direction of an InGaAs-InP platform. This also justifies the need of TM-to-TE mode conversion in a PRS. Finally, we experimentally demonstrate a single-step etched PRS within the same material platform. The waveguides and PRS are designed for operation at λ=6.15 μm at one of the peak mid-IR absorbance wavelengths of ammonia.

The schematic of a single-step etched PRS working at 6.15 μm in the InGaAs-InP platform is illustrated in Fig. 1(a). The waveguides are built on an InP (n=3.07) substrate with a 1.15 μm thick core layer of the InGaAs (n=3.36), and a thin 0.55 μm upper cladding of InP. The PRS operates around the waveguide width w=11 μm where the effective indices (N_{eff}) of the TM_{00} and TE_{10} modes cross, as shown in Fig. 1(b)–1(c). By adiabatically increasing the waveguide width around w=11 μm, the power in the input TM_{00} mode is effectively transferred into the TE_{10} mode due to the mode coupling.[17] Next, the TE_{10} mode is split by a Y-junction splitter into two single-mode TE_{00} modes with 180 degrees phase difference. A 90-degree phase shifter is introduced in the upper arm of the Y-splitter so that the TE_{00} modes are fed into the 2x2 multimode interferometer (MMI), with a total phase difference of 90 degrees. As a result, at the output end, as observed from the three-dimensional (3D) finite difference time domain (FDTD) simulations, the majority of TE_{00} light will output from arm 1 as shown in the Fig. 1(d)–1(g). The PRS has three regions with increasing width taper which are optimized using Lumerical eigenmode expansion solver. In the final design, the pre-converter width increases from 9.8 μm to 10.7 μm over a length of 1 mm, whilst the post-converter width increases from 11.3 μm to 11.75 μm over 0.1 mm length. The primary section of the PRS is the middle converter section which in our design increases in width from 10.7 μm to 11.3 μm. The MMI is 435 μm in length and 22.7 μm in width. The phase shift is generated with waveguides of Bezier curves that give the required 90 degrees phase difference between the two arms. For the characterization of the waveguide devices with end-fire coupling, it is necessary for the two output arms in Fig. 1(a) to be separated by at least 1mm. The separation is achieved by S-bends that extend 2 mm and 0.5 mm along and perpendicular to the propagation direction respectively. As observed in Fig. 1(i), nearly 100% conversion efficiency can be achieved for a pre-converter length of 10 mm and a corresponding converter length ~10mm. From the consideration of epitaxy cost in the preliminary proof-of-concept demonstration, we selected a converter length of 2 mm since the conversion efficiency deviation is relatively small, as observed in Fig. 1(h). The simulation in Fig. 1(h) indicates that 47% conversion efficiency from TM_{00} to TE_{00} can be expected over the total PRS length of 3.04 mm.

Prior to the characterization of the PRS, the propagation loss of the mid-IR InGaAs/InP waveguides was characterized at λ=6.15 μm. 16 waveguides are defined with lengths varying from 25.47 mm to 40.47 mm with 1 mm step by

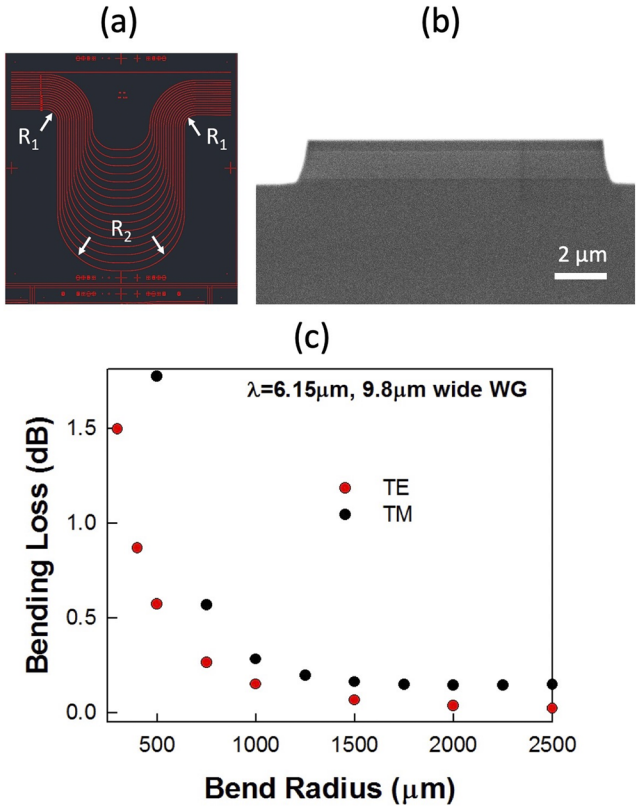

FIG. 2. (a) Layout waveguides for propagation loss measurements, with bending radii R_1 and R_2. (b) SEM cross-section image of the fabricated InGaAs-InP waveguide in the PRS. (c) Bend loss related to modal mismatch at bent and straight interface in a 90-degree bend in a 9.8 μm wide waveguide for the fundamental TE and TM modes at λ=6.15 μm.

adding 500μm long sections on each vertical arm. The layout of the waveguides is as shown in the photomask patterns in Fig. 2(a). Each waveguide has 2 bends with radius R_1 and 2 bends with radius R_2. The total length of each waveguide in the bent regions is constant. The waveguide width is selected as 12 μm. The fabrication of the waveguides is done with photolithography and inductively coupled plasma (ICP) etching with plasma-enhanced chemical vapor deposition (PECVD) silicon oxide as the etching hard mask. A scanning electron microscope (SEM) image of a fabricated waveguide is shown in Fig. 2(b). After fabrication, the waveguides are then cleaved at the two edges and characterized with end-fire coupling setup as shown in Fig. 3. The light from a 6.15 μm QCL is free-space coupled into the waveguides through a lens set. A wire grid polarizer (WGP) is placed between the lens to confirm the polarization states. After routing from the waveguides, light is coupled into a mercury cadmium telluride (MCT) detector via a chalcogenide single mode fiber with a core size of 12 μm. A lock-in amplifier synchronized with the optical chopper, is connected to an MCT detector to read the output optical power. The fiber and the chip are placed on motorized 6-axis stages separately to achieve the best coupling condition. A half wave plate is inserted in the testing setup to enable switching of the input light polarization.

The output transmission of the waveguides with different lengths is measured and the loss at constant input power is plotted. Fig. 3(a) and Fig. 3(b) show the loss versus propagation length difference with input TM_{00} and TE_{00} polarized light respectively at λ=6.15 μm. It should be noted that the last three data points colored in red have a significantly higher loss than the rest of the waveguides. Those three data points correspond to the bottom three waveguides which have a sharp bending radius of 1400, 1200, and 1000 μm (from top to bottom) in Fig. 2(a) are excluded from the propagation loss analysis. The total propagation loss of the waveguide structures comprises the following three terms in Eq. 1.

$$\begin{aligned}\text{Total Loss} = (\#_{interfaces} \times 10log\frac{P_{bend}}{P_{straight}}) \\ + [\pi \times (R_1 + R_2) \times propagation\ loss] \\ + (L \times propagation\ loss)\end{aligned} \quad (1)$$

The first term accounts for the modal mismatch at the interfaces between the bent region and straight region of the waveguides and is defined from the power coupling overlap between bent mode and straight mode. R_1 and R_2 denote respectively the bend radius of the two upper bends and two lower bends in each waveguide in Fig. 2(a). The second term and third term indicate the propagation losses in the bent and straight regions. As shown in Fig. 2(c), when the bending radii are larger than 1500 μm at 6.15 μm wavelength, the additional propagation losses in the bent regions can be neglected. Therefore, they can be treated as typical straight waveguides and we can use the cut-back method to calculate the losses.

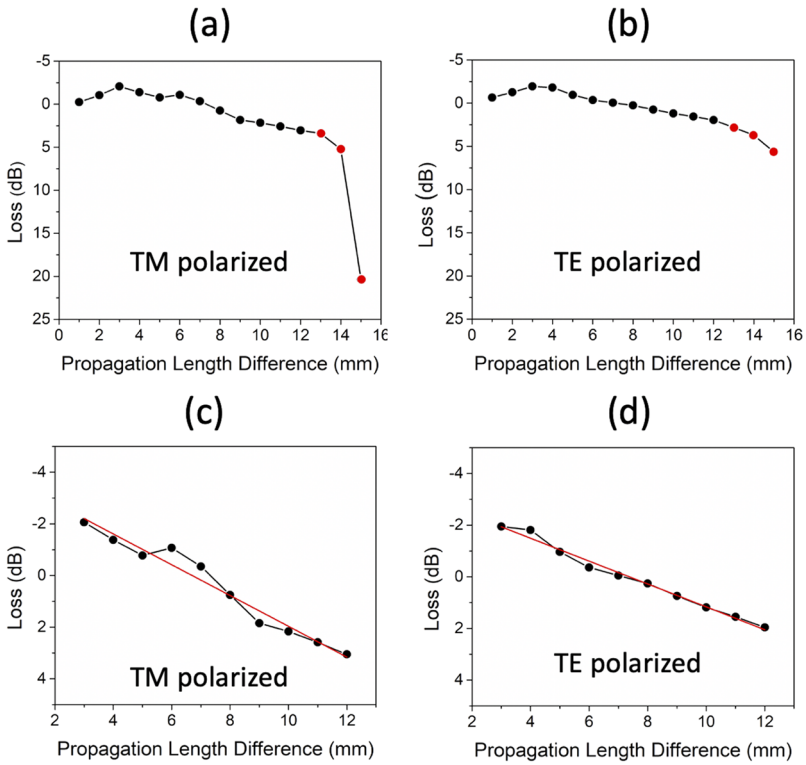

FIG. 3. Loss versus propagation length difference plot for (a) TM polarized input, and (b) TE polarized input. Loss data and linear fitting, excluding waveguides with sharp bends and the linear fitting (shown in red) for (c) TM polarized input, and (d) TE polarized input.

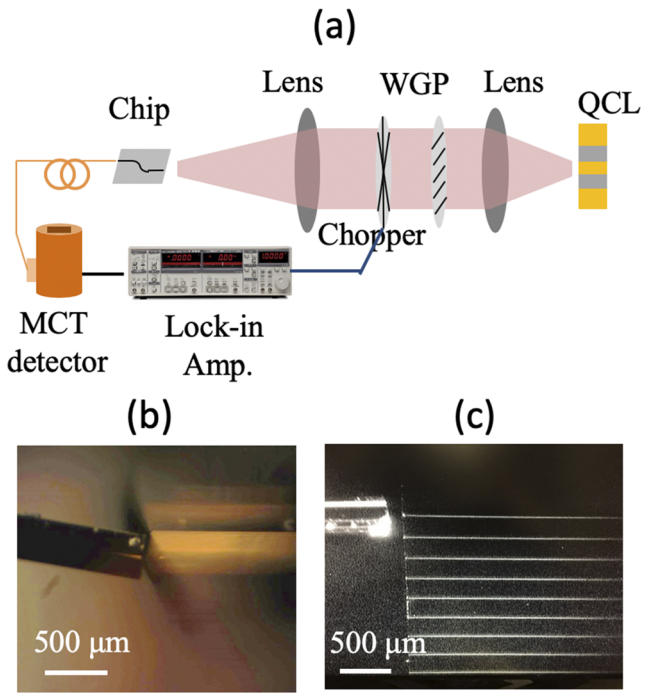

FIG. 4. (a) Schematic plot for testing setup, and (b) (c) images indicates the relative position between fiber and the testing photonic chip from side view and top view cameras respectively.

A linear fitting for propagation loss is done excluding the three data points. From the linear fit, the calculated propagation loss of the waveguide is 4.19 dB/cm for TM mode and 3.25 dB/cm for TE mode as shown in Fig. 3(c)–3(d).

The fabrication of the PRS is also done with photolithography and InP inductively coupled plasma (ICP) etching. The PRS is cleaved and characterized with same end-fire coupling setup as shown in Fig. 4. The width at the output and input cleaved facets in our device is approximately 20 μm. To ensure that only the fundamental modes can propagate, the waveguides are narrowed on the input end of the PRS to 5 μm width (see Fig. 1(c)), so that any modes higher in order than TM_{10}, resulting from the roughness of the cleaved facets, leak into the substrate. By measuring the output power from the two arms of the PRS respectively and calculating the converted TE_{00} power percentage, the polarization conversion efficiency can be known.

Fig. 5 shows the stitched optical microscope image of the fabricated PRS device and the measured results. Four devices with identical geometrical parameters are fabricated and tested. The input optical power focused to the input facet is 1.38 mW. The averaged unconverted TM output light is 58.52 μW and the averaged converted TE output light is 26.51 μW. From strip waveguide measurements, considering the waveguide propagation loss is 4.19 dB/cm for TM and 3.25 dB/cm for TE, the averaged coupling loss of two as-cleaved facets is calculated to be 2.7 dB for TM_{00} mode and 2.78 dB for TE_{00} mode. Therefore, we can estimate the insertion loss of our proposed 3.04 mm long PRS as 4.67 dB which includes ~0.2 dB loss at the MMI[18] and ~1 dB loss at the Y-junction splitter[19] as typically obtained in near-IR measurements. The four PRSs demonstrate an averaged conversion efficiency of 31.2% at the upper arms.

In this paper, a single-step etched polarization rotator-splitter, operating at 6.15 μm wavelength in the InGaAs-InP material system is designed, fabricated and characterized. Simulations indicate that a near 100% conversion efficiency

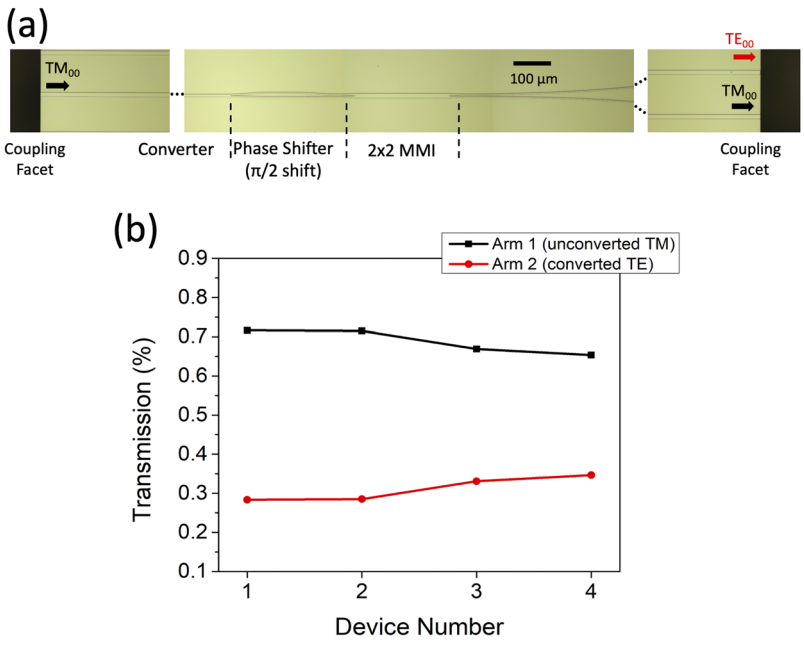

FIG. 5. (a) Stitched optical microscope images of the fabricated PRS, and (b) Transmission of the two output arms for four devices with identical parameters.

can be achieved by the adiabatic transfer of power from the fundamental TM_{00} to TE_{10} mode, with a 10 mm long pre-converter section and a corresponding total converter length ~10mm. Our proof-of-concept device with a total 2 mm long converter section demonstrates experimentally 31.2 % conversion efficiency versus 47 % obtained in simulations. The difference in experimental versus simulated conversion efficiency in our PSR with 2 mm converter length can be attributed to fabrication imperfections, such as deviations in width of the various PRS sections, as well as modal losses at the cleaved facets. Although the single-etched polarization rotator demonstrated here offers ease of fabrication, a device with 100% conversion efficiency would occupy significant area on the chip which translates to higher cost. We have simulated compact polarization rotators with TM_{00} to TE_{00} conversion efficiencies at λ=6.15 μm greater than 90% which can be made in dual-etched (2 mm long)[16] or intrinsic slanted wet etch (230 μm long) configurations[20] and they will be the subjects of future work.

The research was funded by the Army (ARO) STTR Contract #W911NF-17-P-0056. The authors also acknowledge the use of Texas Nanofabrication Facilities supported by the NSF NNCI Award #1542159.

REFERENCES

[1]Y. Zou, S. Chakravarty, C.-J. Chung, X. Xu, and R. T. Chen, "Mid-infrared silicon photonic waveguides and devices [Invited]," Photonics Research **6**, 254–276 (2018).

[2]A. Gurlo and R. Riedel, "In situ and operando spectroscopy for assessing mechanisms of gas sensing," Angewandte Chemie International Edition **46**, 3826–3848 (2007).

[3]M. Lackner, "Tunable diode laser absorption spectroscopy (TDLAS) in the process industries–a review," Reviews in Chemical Engineering **23**, 65–147 (2007).

[4]W.-C. Lai, S. Chakravarty, Y. Zou, and R. T. Chen, "Multiplexed detection of xylene and trichloroethylene in water by photonic crystal absorption spectroscopy," Optics Letters **38**, 3799–3802 (2013).

[5]Y. Zou, S. Chakravarty, P. Wray, and R. T. Chen, "Mid-infrared holey and slotted photonic crystal waveguides in silicon-on-sapphire for chemical warfare simulant detection," Sensors and Actuators B: Chemical **221**, 1094–1103 (2015).

[6]X. Letartre, C. Seassal, C. Grillet, P. Rojo-Romeo, P. Viktorovitch, M. Le Vassor d'Yerville, D. Cassagne, and C. Jouanin, "Group velocity and propagation losses measurement in a single-line photonic-crystal waveguide on InP membranes," Applied Physics Letters **79**, 2312–2314 (2001).

[7]T. Tanemura, I. M. Soganci, T. Oyama, T. Ohyama, S. Mino, K. A. Williams, N. Calabretta, H. J. S. Dorren, and Y. Nakano, "Large-capacity compact optical buffer based on InP integrated phased-array switch and coiled fiber delay lines," Journal of Lightwave Technology **29**, 396–402 (2011).

[8]Y. Ogiso, J. Ozaki, Y. Ueda, N. Kashio, N. Kikuchi, E. Yamada, H. Tanobe, S. Kanazawa, H. Yamazaki, Y. Ohiso, T. Fujii, and M. Kohtoku, "Over 67 GHz bandwidth and 1.5 V Vπ InP-based optical IQ modulator with n-i-p-n heterostructure," Journal of Lightwave Technology **35**, 1450–1455 (2017).

[9]S. Lange, S. Wolf, J. Lutz, L. Altenhain, R. Schmid, R. Kaiser, M. Schell, C. Koos, and S. Randel, "100 GBd intensity modulation and direct detection with an InP-based monolithic DFB laser Mach–Zehnder modulator," Journal of Lightwave Technology **36**, 97–102 (2018).

[10]C. Yu, M. Shangguan, H. Xia, J. Zhang, X. Dou, and J.-W. Pan, "Fully integrated free-running InGaAs/InP single-photon detector for accurate lidar applications," Optics Express **25**, 14611–14620 (2017).

[11]M. Urteaga, Z. Griffith, M. Seo, J. Hacker, and M. J. Rodwell, "InP HBT technologies for THz integrated circuits," Proceedings of the IEEE **105**, 1051–1067 (2017).

[12]Y. Ding, H. Ou, and C. Peucheret, "Wideband polarization splitter and rotator with large fabrication tolerance and simple fabrication process," Optics Letters **38**, 1227–1229 (2013).

[13]M. R. Watts and H. A. Haus, "Integrated mode-evolution-based polarization rotators," Optics Letters **30**, 138–140 (2005).

[14]H. Fukuda, K. Yamada, T. Tsuchizawa, T. Watanabe, H. Shinojima, and S.-i. Itabashi, "Silicon photonic circuit with polarization diversity," Optics Express **16**, 4872–4880 (2008).

[15]Z. Wang and D. Dai, "Ultrasmall Si-nanowire-based polarization rotator," Journal of the Optical Society of America B **25**, 747–753 (2008).

[16]J. Zhang, T.-Y. Liow, M. Yu, G.-Q. Lo, and D.-L. Kwong, "Silicon waveguide based TE mode converter," Optics Express **18**, 25264–25270 (2010).

[17]D. Dai and J. E. Bowers, "Novel concept for ultracompact polarization splitter-rotator based on silicon nanowires," Optics Express **19**(11), 10940–10949 (2011).

[18]A. Hosseini, D. N. Kwong, Y. Zhang, H. Subbaraman, X. Xu, and R. T. Chen, "1× N multimode interference beam splitter design techniques for on-chip optical interconnections," IEEE J. Sel. Top. Quantum Electron. **17**(3), 510–515 (2011).

[19]G. T. Reed, *Silicon Photonics: The State of the Art* (Wiley, 2008).

[20]S. Adachi and H. Kawaguchi, "Chemical etching characteristics of (001) InP," Journal of the Electrochemical Society **128**, 1342–1349 (1981).